Reticular Growth of Graphene Nanoribbon 2D Covalent Organic Frameworks

Gregory Veber[1], Christian S. Diercks[1], Cameron Rogers[1], Wade S. Perkins[1], Jim Ciston[2], Alex Liebman-Peláez[3], Chenhui Zhu[3], Felix R. Fischer[1,4,5,*]

[1]Department of Chemistry, University of California, Berkeley, CA 94720, USA.

[2]National Center for Electron Microscopy, Molecular Foundry, Lawrence Berkeley National Laboratory, Berkeley, CA 94720, USA.

[3]Advanced Light Source, Lawrence Berkeley National Laboratory, Berkeley, CA 94720, USA.

[4]Materials Sciences Division, Lawrence Berkeley National Laboratory, Berkeley, CA 94720, USA.

[5]Kavli Energy NanoSciences Institute at the University of California Berkeley and the Lawrence Berkeley National Laboratory, Berkeley, California 94720, USA.

[*]Correspondence to: ffischer@berkeley.edu

Abstract

The reticular synthesis of covalent organic frameworks (COFs), extended porous two-dimensional (2D) or three-dimensional (3D) networks held together by strong, highly directional chemical bonds, has thus far been restricted to small, shape-persistent, molecular building blocks. Here, we demonstrate the growth of crystalline 2D COFs from a polydisperse macromolecule derived from single-layer graphene, bottom-up synthesized quasi one-dimensional (1D) graphene nanoribbons (GNRs). X-ray scattering and transmission electron microscopy reveal that 2D sheets of GNR-COFs self-assembled at a liquid-liquid interface stack parallel to the layer boundary and exhibit an orthotropic crystal packing. Liquid-phase exfoliation of multilayer GNR-COF crystals gives access to large area (>10^5 nm^2) bilayer and trilayer cGNR-COF films. The functional integration of extended 1D materials into crystalline COFs greatly expands the structural complexity and the scope of mechanical and physical materials properties accessible through a deterministic reticular bottom-up approach.

One Sentence Summary

Reticular growth at a liquid-liquid interface directs the self-assembly of graphene nanoribbons into highly anisotropic crystalline 2D covalent organic frameworks.

Introduction, Results, and Discussion

Covalent organic frameworks (COFs) are 2D or 3D extended periodic networks assembled from symmetric, shape persistent molecular building blocks through strong, directional bonds [1,2]. Traditional COF growth strategies heavily rely on reversible condensation reactions that guide the reticulation toward a desired thermodynamic equilibrium structure [3]. The requirement for dynamic error correction, however, limits the choice of building blocks and thus the associated mechanical and electronic properties imbued within the periodic lattice of the COF. Furthermore, the poor electronic communication across imine and boronate ester linkers, most commonly used in the synthesis of 2D COFs, gives rise to semiconducting materials featuring large band gaps undesirable for advanced electronic applications [4,5]. Charge-carrier transport in these materials is dominated by interlayer hopping mechanisms rather than through chemical bonds between linkers and the constituent molecular building blocks within a 2D sheet [6]. Introduction of conjugated polymers as 1D conduction paths within a single COF sheet could address this shortcoming, yet the incorporation of macromolecules as building units in COFs has not been demonstrated. Recent advances in the bottom-up synthesis of graphene nanoribbons (GNRs), atomically thin quasi one-dimensional (1D) strips of graphene, have inspired the development of a new class of COF building blocks. The control over key structural parameters in GNRs, width [7–10], edge symmetry [7,11,12], dopant atom density [13–15], and dopant position [16,17] gives rise to a highly tunable band structure and the emergence of exotic physical phenomena linked to symmetry protected topological states [18,19]. Here we show that the exquisite structural control inherent to bottom-up synthesized GNRs can be

adapted to introduce atomically precise spacings of functional groups along the edges of a ribbon, giving access to a shape persistent quasi-1D macromolecular building block for the reticular synthesis of 2D COFs.

Imine linked GNR-COF films were assembled from aldehyde functionalized cove-GNRs (CHO-cGNR) and benzidine crosslinkers. Large area, homogenous thin-films of variable thickness were synthesized through interfacial polymerization at a liquid-liquid interface. By modulating the concentration of GNRs in the reaction mixture the film thickness can be controlled over a range of 2–22 nm. Fourier transform infrared (FT-IR) spectroscopy along with control experiments using unfunctionalized cGNRs confirmed that the GNR-COF films are covalently linked through imine bonds. The crystallographic structure of the GNR-COF was probed using wide angle X-ray scattering (WAXS) and transmission electron microscopy (TEM), revealing the extraordinary potential of reticular covalent self-assembly techniques to access densely packed parallel arrays of GNRs. Liquid-phase exfoliation of crystalline cGNR-COFs gives access to vertically stacked few-layered cGNR-COF flakes for applications in functional materials and advanced electronics.

The synthesis of CHO-cGNRs is depicted in Fig. 1A. Diels-Alder polymerization of acetal protected cyclopentadienone **3** yields the *poly*-phenylene precursor **4**. Size exclusion chromatography (SEC) shows a bimodal distribution of linear polymers (M_n = 26,000 g mol^{-1}) and cyclic oligomers (M_n = 3,000 g mol^{-1}) (Fig. S1) characteristic for a step-growth polymerization mechanism [20,21]. Acid catalyzed deprotection of crude **4** yields the aldehyde functionalized *poly*-phenylene **5**. Fractionation of the polymer mixture by preparative SEC gave access to samples of high molecular weight linear polymer **5** (M_n = 18,500 g mol^{-1}) and low molecular weight cyclic oligomers (M_n = 2,100 g mol^{-1}) (Fig. 1B). MALDI mass spectroscopy of linear polymers **4** and **5** shows families of molecular ions separated by the repeat unit of the polymers, 676 g mol^{-1} and

588 g mol^{-1} for **4** and **5**, respectively (Fig. 1C). The successful deprotection of **4** is further corroborated by the absence of characteristic peaks associated with the acetal protecting group (δ = 4.16–3.89 ppm) in ^{1}H-NMR spectra of **5** and the appearance of a new peak consistent with the aldehyde group hydrogen atoms (δ = 10.06–9.85 ppm) (Fig. S2). Oxidative cyclodehydrogenation of **5** yields CHO-cGNR as a dark solid. Raman spectra of CHO-cGNRs show the characteristic signatures of cGNRs; a radial breathing like mode (RBLM) (253 cm^{-1}), the D (1332 cm^{-1}), and the G (1603 cm^{-1}) peaks as well as overtone 2D, D+D$^{'}$, and 2D$^{'}$ peaks (Fig. 1D) [20,22,23]. An overlay of the respective IR spectra of *poly*-phenylene **5** and CHO-cGNR confirms the presence of aldehyde groups in the GNRs. The relative intensity of the characteristic aldehyde C=O stretching mode at 1699 cm^{-1}, with respect to the C=C stretching mode at 1602 cm^{-1}, remains unchanged following the oxidative cyclodehydrogenation (Fig. 1E). The UV/vis absorption spectrum of aldehyde functionalized CHO-cGNRs, indistinguishable from an original sample of cGNRs featuring solubilizing alkyl chains (Fig. S3) [23], along with the characteristic Raman spectra (Fig. 1D), is further evidence that the oxidative cyclodehydrogenation proceeds to the expected high degree of conversion [20,23].

Imine cross-linked crystalline cGNR-COFs were grown using a Lewis acid catalyzed interfacial polymerization[24–26]. The physical separation of the catalyst ($Sc(OTf)_3$), dissolved in an aqueous phase, and the organic building blocks, CHO-cGNRs and the benzidine cross-linker dispersed in an immiscible organic phase, relegate the COF film growth exclusively to the liquid-liquid interface. The limited stability of dispersions of CHO-cGNRs in a wide variety of solvents along with the requirement that the density of the organic phase be greater than the aqueous phase to prevent the undesired precipitation of amorphous GNR aggregates at the liquid-liquid interface during film growth, narrowed the selection of organic solvents to mixtures of *o*-dichlorobenzene

(*o*-DCB) and chloroform. High quality cGNR-COFs were obtained by layering an aqueous solution of $Sc(OTf)_3$ (5 mM) over a homogenous dispersion of CHO-cGNRs and benzidine in *o*-DCB/$CHCl_3$ (*v*/*v* = 1:1). Over the course of 5–7 days gray films form at the liquid-liquid boundary that were scooped from the interface and transferred onto solid substrates (Fig 2A). A series of control experiments that alternately remove any one of the critical components, CHO-cGNRs, benzidine cross-linker, or $Sc(OTf)_3$, from the reaction mixture preclude the formation of cGNR-COFs even after extended reaction times. Similarly, the replacement of CHO-cGNRs with unfunctionalized cGNRs did not lead to the formation of COF films at the liquid-liquid interface (Fig. S4). We therefore conclude that the observed cGNR-COF films formed in the presence of both reaction partners, CHO-cGNRs, benzidine, and the Lewis acid catalyst are not comprised of non-covalently assembled films formed at the interface solely driven by π-π interactions.

Optical microscopy of cGNR-COFs transferred onto a Si/SiO_2 surface reveal large flakes (> 1000 μm^2) of uniform color contrast (Fig. 2B). Raman spectra recorded at various positions on cGNR-COF films show the characteristic RBLM, D, and G peaks associated with CHO-cGNRs, supporting the structural assignment (Fig. 2C, blue and red trace). Areas of the SiO_2 apparently devoid of cGNR-COFs show only very weak Raman signatures (Fig. 2C, black trace), attributed to small GNR aggregates or individual ribbons transferred with the solvent during the scooping process. Spatial Raman maps of the G-peak intensity of cGNR-COFs on Si/SiO_2 seamlessly coincide with the optical contrast in microscopy images (Fig. S5). Attenuation of the FT-IR spectra recorded on transferred cGNR-COFs reveal the formation of imine bonds within the film. The FT-IR spectrum of the cGNR-COF, as compared to the CHO-cGNR, shows a decrease in the intensity of the characteristic aldehyde C=O stretching mode (λ^{-1} = 1702 cm^{-1}) relative to the C=C mode (λ^{-1} = 1600 cm^{-1}) (Fig. 1E). The imine C=N stretching mode resulting from the crosslinking of

CHO-cGNRs with benzidine appears as a new shoulder at λ^{-1} = 1657 cm^{-1} in the IR spectrum of cGNR-COFs (Fig. 1E).

cGNR-COF film morphology and thickness were examined using scanning electron microscopy (SEM) and atomic force microscopy (AFM). SEM images of cGNR-COF films transferred onto TEM grids show large-scale homogeneity and well-defined film morphology (Fig. 2D). Large areas (> 100 μm^2) of homogenous, smooth films show little to no amorphous regions or protrusions from the surface (Fig. 2D). This is further supported by ambient AFM that shows films with height profiles ranging from 2–20 nm (Fig. 2E, Fig. S6). The thickness of cGNR-COF films prepared through Lewis acid catalyzed growth at the liquid-liquid interface scales linearly with the initial concentration of CHO-cGNRs (Fig. S7). Dilute dispersions of CHO-cGNRs (67 μg mL^{-1}) yield film thicknesses as low as 2 nm while higher concentrations (270 μg mL^{-1}) form films with average thicknesses in excess of 20 nm.

We used synchrotron X-ray scattering to study the crystallographic structure of cGNR-COFs films. Fig. 3A shows the projected trace of the wide-angle X-ray scattering (WAXS) pattern of powdered samples of cGNR-COFs grown at the liquid-liquid interface. The data was collected by suspending a dried, powdered sample of cGNR-COFs in a quartz capillary perpendicular to the incident beam. The WAXS pattern shows three characteristic reflections at 2θ = 3.5°, 7.0°, and 12.0° corresponding to *d*-spacings of 2.5 nm, 1.2 nm, and 0.7 nm, respectively (Fig. 3A). A structure model for the packing of cGNR-COF constructed in the triclinic space group *P*–1 with unit cell parameters a = 5.0 Å, b = 7.4 Å, c = 25.5 Å, α = 100°, β = 90°, and γ = 90° is depicted in Fig 3B. The predicted diffraction pattern is in good agreement with experimental data. The observed reflections at 2.5 nm, 1.2 nm, and 0.7 nm were assigned to the (001), (002), and (01–1) planes, respectively (Fig. 3A). The (001) and (002) Bragg reflections correspond to the distance,

and half the distance, between parallel ribbons (2.5 nm and 1.25 nm) whereas the (01–1) corresponds to the spacing of benzidine linkers (0.7 nm) lining the edges of the cGNRs (Fig. 3B). The Bragg reflections associated with the interlayer π-stacking between cGNRs is masked by the pronounced background of the quartz capillary in the expected region of the WAXS pattern.

We used high-resolution transmission electron microscopy (HR-TEM) to study the crystalline domain size of cGNR-COF films directly scooped from the liquid-liquid interphase (Fig. 3C). The micrographs, recorded at a total electron dose of 100 e $Å^{-2}$ to minimize sample damage, display clear lattice fringes corresponding to the distance between linkers (0.7 nm) (Fig. 3D) and the π-stacking between ribbons (0.35 nm) (Fig. 3E), respectively. The observed lattice fringes corroborate the molecular model depicted in Fig. 3B and can be assigned to the (01–1) and (105) lattice planes, respectively. The fact that the (001) and (002) planes related to the distance between covalently linked cGNRs cannot be observed in the TEM images is attributed to a preferential orientation of the crystallites within the film relative to the TEM grid. Following the scooping transfer the cGNR-COFs adopt orientations in which the lateral spacing between cGNRs (2.5 nm) lies on an axis perpendicular to the surface and remains out of focus leaving only the π-stacking and linker-linker distances to be observed by in-plane elastic scattering. Most notably, the HR-TEM demonstrates that the crystalline domain size (> 400 nm^2) is 1–2 orders of magnitude larger than previously reported solution processable GNR films formed via π-stacking alone [27]. cGNR-COFs not only self-assemble into larger crystallites but macromolecular reticulation through directional covalent bonds allows for the rational design of highly anisotropic materials.

Finally, adopting a liquid-phase exfoliation protocol for the delamination of crystalline 2D COFs, we were able to access free-standing few-layer 2D cGNR-COF sheets. A dispersion of multilayer films grown from a saturated CHO-cGNR solution in acetone was transferred to *o*-

DCB, sonicated, and drop-cast onto Si/SiO_2. The resulting cGNR-COF flakes were analyzed using ambient AFM to determine the film thickness, size, and homogeneity (Fig. 4, A and B). The lateral dimensions of the cGNR-COF flakes are > 10^5 nm^2 and range in thickness between 0.70 nm (Fig. 4C) and 1.05 nm (Fig. 4D), corresponding to bilayer and trilayer stacks of 2D cGNR-COF sheets (π-π-stacking distance Δ = 0.35 nm). Some exfoliated films exhibit layered height profiles commensurate with step-edges within a single flake (Fig. S8). The orthotropic crystal packing adopted by GNRs in 2D COF films represents a unique opportunity to enhance the chemical, physical, and optoelectronic properties of COFs by independently tuning the mechanical and electrical material properties along all three axes of the crystal lattice. The simplicity of our interfacial GNR-COF growth and liquid-phase exfoliation protocol opens the path to accessing densely packed 2D sheets of parallel GNRs for high-performance electronic device architectures and the exploration of exotic physical phenomena emerging from deterministically engineered stacks of anisotropic layered 2D materials.

References

(1) Diercks, C. S.; Yaghi, O. M. The Atom, the Molecule, and the Covalent Organic Framework. *Science* **2017**, *355*, 6328.

(2) Colson, J. W.; Dichtel, W. R. Rationally Synthesized Two-Dimensional Polymers. *Nat. Chem.* **2013**, *5*, 453–465.

(3) Smith, B. J.; Overholts, A. C.; Hwang, N.; Dichtel, W. R. Insight into the Crystallization of Amorphous Imine-Linked Polymer Networks to 2D Covalent Organic Frameworks. *Chem. Commun.* **2016**, *52*, 3690–3693.

(4) Joshi, T.; Chen, C.; Li, H.; Diercks, C. S.; Wang, G.; Waller, P. J.; Li, H.; Bredas, J. L.; Yaghi, O. M.; Crommie, M. F. Local Electronic Structure of Molecular Heterojunctions in a Single-Layer 2D Covalent Organic Framework. *Adv. Mater.* **2019**, *31*, 6–11.

(5) Chen, C.; Joshi, T.; Li, H.; Chavez, A. D.; Pedramrazi, Z.; Liu, P. N.; Li, H.; Dichtel, W. R.; Bredas, J. L.; Crommie, M. F. Local Electronic Structure of a Single-Layer Porphyrin-Containing Covalent Organic Framework. *ACS Nano* **2018**, *12*, 385–391.

(6) Dogru, M.; Bein, T. On the Road towards Electroactive Covalent Organic Frameworks. *Chem. Commun.* **2014**, *50*, 5531–5546.

(7) Cai, J.; Ruffieux, P.; Jaafar, R.; Bieri, M.; Braun, T.; Blankenburg, S.; Muoth, M.; Seitsonen, A. P.; Saleh, M.; Feng, X.; Müllen, K.; Fasel, R. Atomically Precise Bottom-up Fabrication of Graphene Nanoribbons. *Nature* **2010**, *466*, 470–473.

(8) Chen, Y. C.; De Oteyza, D. G.; Pedramrazi, Z.; Chen, C.; Fischer, F. R.; Crommie, M. F. Tuning the Band Gap of Graphene Nanoribbons Synthesized from Molecular Precursors. *ACS Nano* **2013**, *7*, 6123–6128.

(9) Talirz, L.; De, H. S.; Dumsla, T.; Wang, S.; Sanchez-valencia, J. R.; Liu, J.; Shinde, P.; Pignedoli, C. A.; Liang, L.; Meunier, V.; Plumb, N. C.; Shi, M.; Feng, X.; Narita, A.; Müllen, K.; Fasel, R.; Ruffieux, P. On-Surface Synthesis and Characterization of 9 - Atom Wide Armchair Graphene Nanoribbons. *ACS Nano* **2017**, *11*, 1380–1388.

(10) Zhang, H.; Lin, H.; Sun, K.; Chen, L.; Zagranyarski, Y.; Aghdassi, N.; Duhm, S.; Li, Q.; Zhong, D.; Li, Y.; Müllen, K.; Fuchs, H.; Chi, L. On-Surface Synthesis of Rylene-Type Graphene Nanoribbons. *J. Am. Chem. Soc.* **2015**, *137*, 4022–4025.

(11) Liu, J.; Li, B.-W.; Tan, Y.; Giannakopoulos, A.; Sanchez-Sanchez, C.; Beljonne, D.; Ruffieux, P.; Fasel, R.; Feng, X.; Müllen, K. Towards Cove-Edged Low Band Gap Graphene Nanoribbons. *J. Am. Chem. Soc.* **2015**, *137*, 6097–6103.

(12) Ruffieux, P.; Wang, S.; Yang, B.; Sanchez-Sanchez, C.; Liu, J.; Dienel, T.; Talirz, L.; Shinde, P.; Pignedoli, C. A.; Passerone, D.; Dumslaff, T.; Feng, X; Müllen, K.; Fasel, R. On-Surface Synthesis of Graphene Nanoribbons with Zigzag Edge Topology. *Nature* **2016**, *531*, 489–492.

(13) Cai, J.; Pignedoli, C. A.; Talirz, L.; Ruffieux, P.; Söde, H.; Liang, L.; Meunier, V.; Berger, R.; Li, R.; Feng, X.; Müllen, K; Fasel, R. Graphene Nanoribbon Heterojunctions. *Nat. Nanotechnol.* **2014**, *9*, 896–900.

(14) Bronner, C.; Stremlau, S.; Gille, M.; Brauße, F.; Haase, A.; Hecht, S.; Tegeder, P. Aligning the Band Gap of Graphene Nanoribbons by Monomer Doping. *Angew. Chemie - Int. Ed.* **2013**, *52*, 4422–4425.

(15) Zhang, Y.; Zhang, Y.; Li, G.; Lu, J.; Lin, X.; Du, S.; Berger, R.; Feng, X.; Müllen, K.; Gao, H. J. Direct Visualization of Atomically Precise Nitrogen-Doped Graphene Nanoribbons. *Appl. Phys. Lett.* **2014**, *105*.

(16) Cloke, R. R.; Marangoni, T.; Nguyen, G. D.; Joshi, T.; Rizzo, D. J.; Bronner, C.; Cao, T.; Louie, S. G.; Crommie, M. F.; Fischer, F. R. Site-Specific Substitutional Boron Doping of Semiconducting Armchair Graphene Nanoribbons. *J. Am. Chem. Soc.* **2015**, *137*, 8872–8875.

(17) Durr, R. A.; Haberer, D.; Lee, Y. L.; Blackwell, R.; Kalayjian, A. M.; Marangoni, T.; Ihm, J.; Louie, S. G.; Fischer, F. R. Orbitally Matched Edge-Doping in Graphene Nanoribbons. *J. Am. Chem. Soc.* **2018**, *140*, 807–813.

(18) Rizzo, D. J.; Veber, G.; Cao, T.; Bronner, C.; Chen, T.; Zhao, F.; Rodriguez, H.; Louie, S. G.; Crommie, M. F.; Fischer, F. R. Topological Band Engineering of Graphene Nanoribbons. *Nature* **2018**, *560*, 204–208.

(19) Gröning, O.; Wang, S.; Yao, X.; Pignedoli, C. A.; Borin Barin, G.; Daniels, C.; Cupo, A.; Meunier, V.; Feng, X.; Narita, A.; Müllen, K; Ruffieux, P.; Fasel, R. Engineering of

Robust Topological Quantum Phases in Graphene Nanoribbons. *Nature* **2018**, *560*, 209–213.

(20) Narita, A.; Feng, X.; Hernandez, Y.; Jensen, S. A.; Bonn, M.; Yang, H.; Verzhbitskiy, I. A.; Casiraghi, C.; Hansen, M. R.; Koch, A. H. R.; Fytas, G.; Ivasenko, O.; Li, B.; Mali, K. S.; Balandina, T; Mahesh, S.; De Feyter, S.; Müllen, K. Synthesis of Structurally Well-Defined and Liquid-Phase-Processable Graphene Nanoribbons. *Nat. Chem.* **2014**, *6*, 126–132.

(21) Narita, A.; Verzhbitskiy, I. A.; Frederickx, W.; Mali, K. S.; Jensen, S. A.; Hansen, M. R.; Bonn, M.; De Feyter, S.; Casiraghi, C.; Feng, X.; Müllen, K. Bottom-up Synthesis of Liquid-Phase-Processable Graphene Nanoribbons with near-Infrared Absorption. *ACS Nano* **2014**, *8*, 11622–11630.

(22) Joshi, D.; Hauser, M.; Veber, G.; Berl, A.; Xu, K.; Fischer, F. R. Super-Resolution Imaging of Clickable Graphene Nanoribbons Decorated with Fluorescent Dyes. *J. Am. Chem. Soc.* **2018**, 140, 9574–9580.

(23) Perkins, W.; Fischer, F. R. Inserting Porphyrin Quantum Dots in Bottom-Up Synthesized Graphene Nanoribbons. *Chem. Eur. J.* **2017**, *23*, 17687–17691.

(24) Sahabudeen, H.; Qi, H.; Glatz, B. A.; Tranca, D.; Dong, R.; Hou, Y.; Zhang, T.; Kuttner, C.; Lehnert, T.; Seifert, G.; Kaiser, U.; Fery, A.; Zheng, Z; Feng, X. Wafer-Sized Multifunctional Polyimine-Based Two-Dimensional Conjugated Polymers with High Mechanical Stiffness. *Nat. Commun.* **2016**, *7*, 1–8.

(25) Dai, W.; Shao, F.; Szczerbiński, J.; McCaffrey, R.; Zenobi, R.; Jin, Y.; Schlüter, A. D.; Zhang, W. Synthesis of a Two-Dimensional Covalent Organic Monolayer through Dynamic Imine Chemistry at the Air/Water Interface. *Angew. Chemie - Int. Ed.* **2016**, *55*, 213–217.

(26) Matsumoto, M; Valentino, L; Stiehl, G. M.; Balch, H. B.; Corcos, A. R.; Wang, F; Ralph, D. C.; Mariñas, B. J.; Dichtel, W. R.. Lewis-Acid-Catalyzed Interfacial Polymerization of Covalent Organic Framework Films. *Chem* **2018**, *4*, 308–317.

(27) Shekhirev, M.; Vo, T. H.; Pour, M. M.; Sinitskii, A.; Munukutla, S.; Lyding, J. W. Interfacial Self-Assembly of Atomically Precise Graphene Nanoribbons into Uniform Thin Films for Electronics Applications. *ACS Appl. Mater. Interfaces* **2017**, *9*, 693–700.

Acknowledgments:

Funding

Research supported by the Office of Naval Research MURI Program N00014-16-1-2921 (molecular synthesis, characterization, and COF film growth), and the Center for Energy Efficient

Electronics NSF Award 0939514 (GNR synthesis and characterization); research used beamline 7.3.3 of the Advanced Light Source, which is a DOE Office of Science User Facility under contract no. DE-AC02-05CH11231 (WAXS); work at the Molecular Foundry (NCEM) was supported by the Office of Science, Office of Basic Energy Sciences, of the U.S. Department of Energy under Contract No. DE-AC02-05CH11231 (TEM);

Author contributions

G.V. and F.R.F conceived the experiments. G.V. performed synthesis, COF growth, sample preparation, characterization, and data analysis. G. V. and C.R. performed SEM. G. V. and W. S. P. performed ambient AFM. C.Z. and A.L.-P. performed X-ray diffraction. C.S.D. performed diffraction data analysis and modeling. J.C. performed TEM. G.V., C.S.D., and F.R.F contributed to writing of the paper.

Competing interests

The authors declare no competing interests

Data and materials availability

All data are available in the main text or the Supplementary Materials.

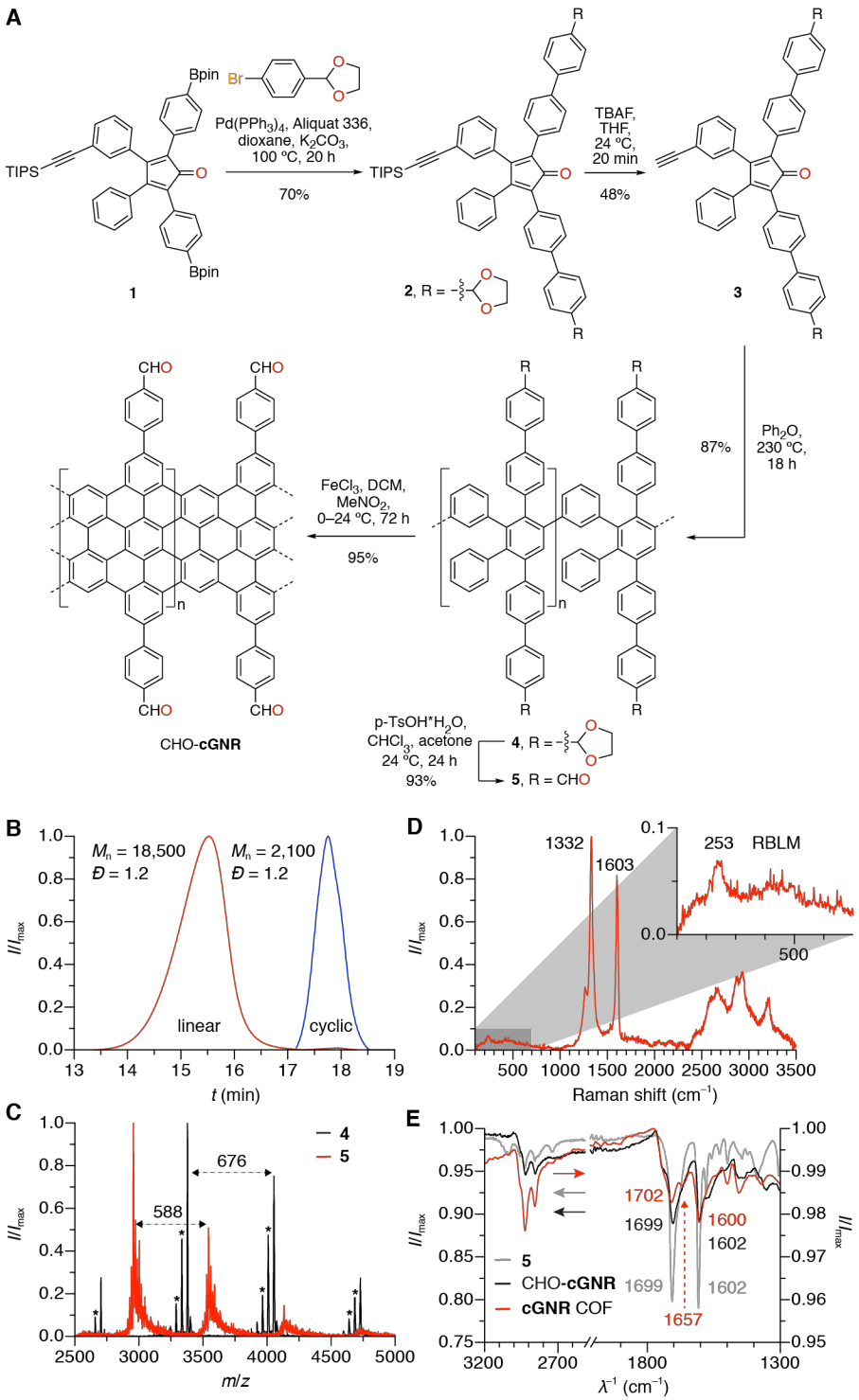

Figure 1. **Synthesis and characterization of aldehyde-functionalized CHO-cGNRs.** (A) Schematic representation of the synthesis of CHO-cGNR. (B) SEC traces for the linear polymers (red) and cyclic oligomers (blue) of **5**. (C) MALDI mass spectrum of crude **4** (black) and **5** (red) showing families of molecular ions separated by the mass of each polymer repeat unit (*

corresponds to subfamilies of molecular ions resulting from the loss of acetal protecting groups). (D) Raman spectrum (λ_E = 532 nm) of CHO-cGNRs. Inset shows the characteristic RLBM of cGNRs. (E) FT-IR spectrum of **5** (gray), CHO-cGNRs (black), and cGNR-COF (red) showing the characteristic aldehyde C=O (λ^{-1} = 1699 cm^{-1}) and aromatic C=C (λ^{-1} = 1602 cm^{-1}) stretching modes in both **5** and CHO-cGNRs. The IR spectrum of cGNR-COF shows a decrease in the intensity of the aldehyde C=O (λ^{-1} = 1702 cm^{-1}) relative to the C=C mode (λ^{-1} = 1600 cm^{-1}) along with the signal for the C=N imine stretching mode (λ^{-1} = 1657 cm^{-1}).

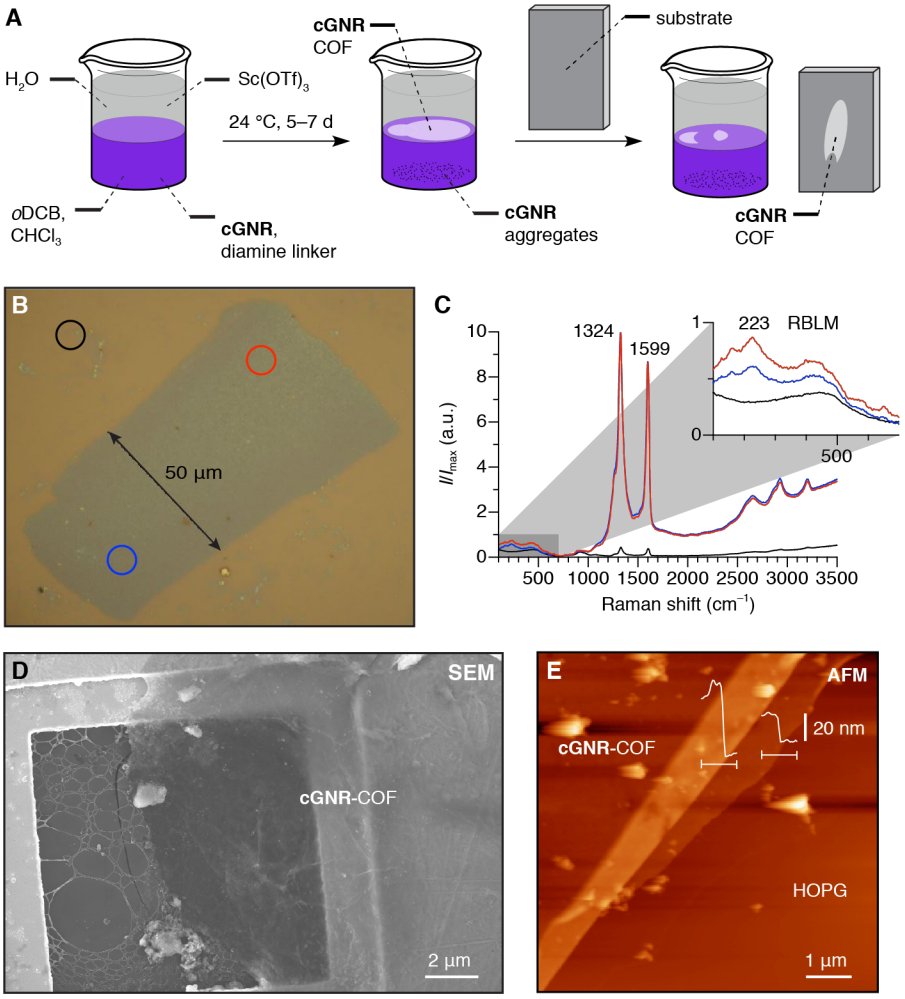

Figure 2. Synthesis and characterization of cGNR-COF thin films. (A) Schematic representation of the interfacial polymerization and scooping transfer process. (B) Optical

microscopy image of a transferred cGNR-COF film on Si/SiO_2. Circles correspond to positions where Raman spectra were recorded. (C) Raman spectra (λ_E = 532 nm) of the three regions highlighted in (B). Inset shows the characteristic RLBM. (D) Scanning electron microscopy (SEM) image of cGNR-COF film dispersion dropcast onto a TEM grid (5 kV accelerating voltage). (E) Atomic force microscopy (AFM) of ~20 nm cGNR-COF film on HOPG. Film thickness in folded regions corresponds to integer multiples of the single layer film (~40 nm).

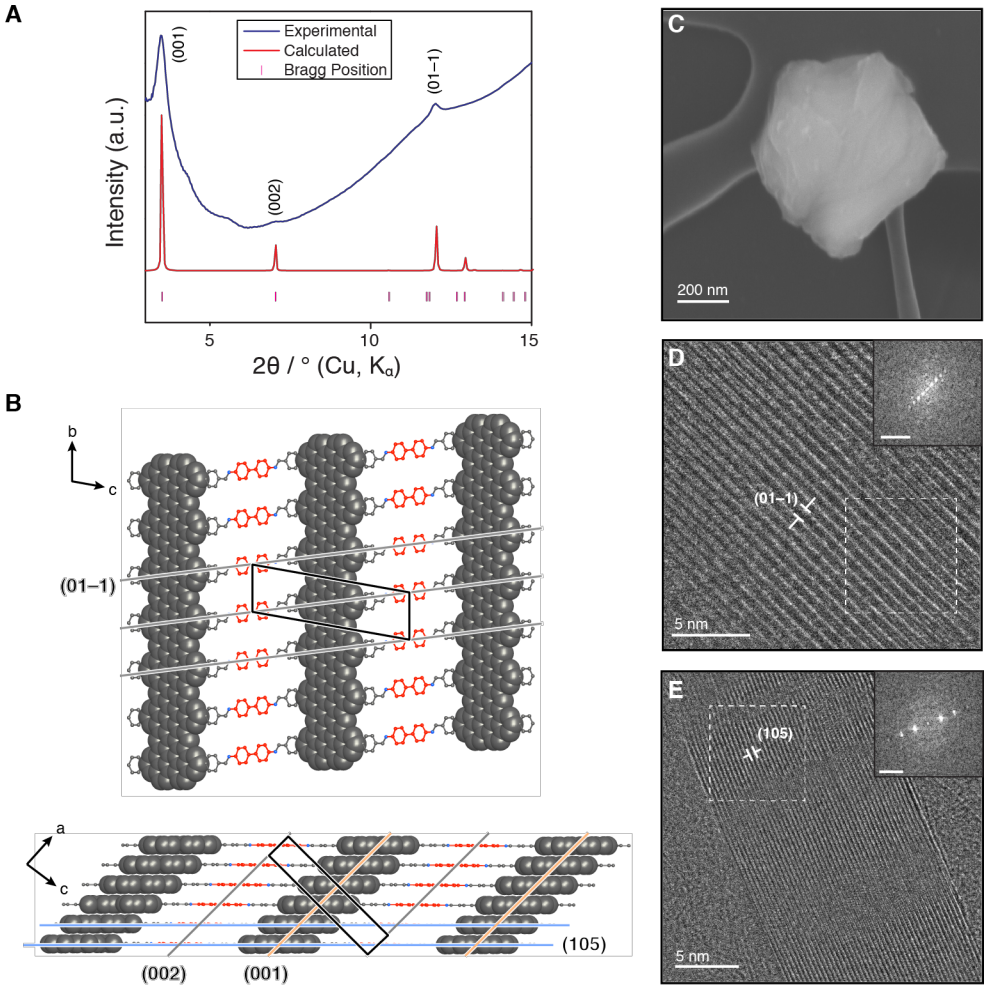

Figure 3. Powder X-ray diffraction and HR-TEM of cGNR-COF thin films. (A) Experimentally and theoretically calculated WAXS pattern of powdered sample of cGNR-COF film. (B) Structural model of cGNR-COF with unit cell (black box), orientation displaying lattice

plane (01–1) corresponding to distance between linkers (0.7 nm) (top), orientation displaying interlayer packing and lattice planes (001) (orange), (002) (gray), and (105) (blue) corresponding to 2.5 nm, 1.25 nm, and 0.35 nm (bottom). (C) SEM image of cGNR-COF film from HR-TEM sample. (D) HR-TEM image of cGNR-COF crystallite displaying the (01–1) plane, fringes separated by 0.7 nm (white marker), Fourier diffractogram of the highlighted region (inset, scale bar 5 nm^{-1}). (E) HR-TEM image of cGNR-COF crystallite displaying the (105) plane, fringes represent π-π-stacking (0.35 nm) within the film, Fourier diffractogram of the highlighted region (inset, scale bar 5 nm^{-1}).

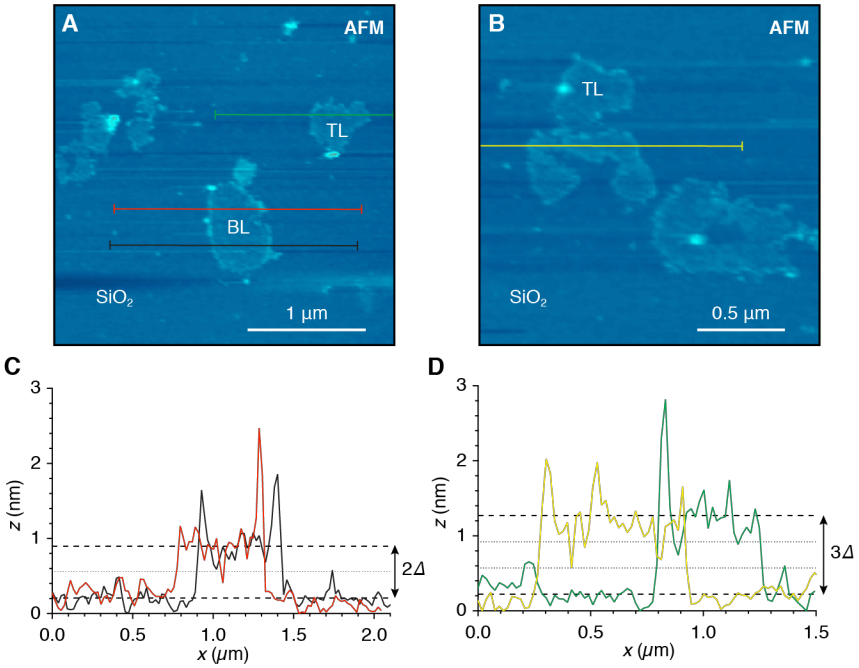

Figure 4. Chemically exfoliated bilayer and trilayer cGNR-COF flakes on SiO_2 substrates. (A–B) AFM topographic images of liquid-phase exfoliated cGNR-COF on SiO_2. (C–D) AFM *z*-height profiles along the lines depicted in A,B. Averaged background and averaged plateau height (black dashed lines), spacing corresponding to interlayer π-π-stacking distance (Δ = 0.35 nm) as determined via HR-TEM and diffraction models (grey dotted lines).

Supplementary Materials

Reticular Growth of Graphene Nanoribbon Covalent Organic Frameworks

Gregory Veber[1], Christian S. Diercks[1], Cameron Rogers[1], Wade S. Perkins[1], Jim Ciston[2], Alex Liebman-Peláez[3], Chenhui Zhu[3], Felix R. Fischer[1,4,5,*]

[1]Department of Chemistry, University of California, Berkeley, CA 94720, USA.

[2]National Center for Electron Microscopy, Molecular Foundry, Lawrence Berkeley National Laboratory, Berkeley, CA 94720, USA.

[3]Advanced Light Source, Lawrence Berkeley National Laboratory, Berkeley, CA 94720, USA.

[4]Materials Sciences Division, Lawrence Berkeley National Laboratory, Berkeley, CA 94720, USA.

[5]Kavli Energy NanoSciences Institute at the University of California Berkeley and the Lawrence Berkeley National Laboratory, Berkeley, California 94720, USA.

[*]Correspondence to: ffischer@berkeley.edu

Materials and Methods Unless otherwise stated, all manipulations of air and/or moisture sensitive compounds were carried out in oven-dried glassware, under an atmosphere of N_2 or Ar. All solvents and reagents were purchased from Alfa Aesar, Spectrum Chemicals, Acros Organics, TCI America, and Sigma-Aldrich and were used as received unless otherwise noted. Organic solvents were dried by passing through a column of alumina and were degassed by vigorous bubbling of N_2 or Ar through the solvent for 20 min. Flash column chromatography was performed on SiliCycle silica gel (particle size 40–63 μm). Thin layer chromatography was performed using SiliCycle silica gel 60 Å F-254 precoated plates (0.25 mm thick) and visualized by UV absorption. HOPG substrates were purchased from SPI supplies (3 mm Grade SPI-3). All ^{1}H and ^{13}C NMR spectra were recorded on Bruker AV-300, AVB-400, AV-600, DRX-500, and AV-500 MHz spectrometers, and are referenced to residual solvent peaks ($CDCl_3$ ^{1}H NMR = 7.26 ppm, ^{13}C NMR = 77.16 ppm; CD_2Cl_2 ^{1}H NMR = 5.32 ppm, ^{13}C NMR = 53.84 ppm). ESI mass spectrometry was performed on a Finnigan LTQFT (Thermo) spectrometer in positive ionization mode. MALDI mass spectrometry was performed on a Voyager-DE PRO (Applied Biosystems Voyager System 6322) in positive mode using a matrix of dithranol. Gel permeation chromatography (GPC) was carried out on a LC/MS Agilent 1260 Infinity set up with a guard and two Agilent Polypore 300 × 7.5 mm columns at 35 °C. All GPC analyses were performed on a 0.2 mg mL^{-1} solution of polymer in $CHCl_3$. An injection volume of 25 μL and a flow rate of 1 mL min^{-1} were used. Calibration was based on narrow polydispersity polystyrene standards ranging from M_w = 100 to 4,068,981 au. Raman spectroscopy was performed on a Horiba Jobin Yvon LabRAM ARAMIS confocal Raman microscope with 532 nm excitation wavelength. Wide-angle X-ray scattering (WAXS) data was acquired on beamline 7.3.3 at the Advanced Light Source with a Pilatus 2M detector. Powder samples were dropcast from acetone, dried in quartz capillaries and put into a helium atmosphere for measurement in transmission geometry. Silver behenate was used for calibration. The Nika package for IGOR Pro (Wavemerics) was used to reduce the acquired 2D raw data to a 1D profile[1]. SEM was performed on a Zeiss Gemini Ultra-55 FESEM with an accelerating voltage between 2–10 kV. Low-dose HR-TEM images were acquired on the TEAM I instrument at the National Center for Electron Microscopy at the Molecular Foundry. TEAM I is an FEI Titan-class microscope operated at 300 kV, with geometric aberrations corrected to third order (with partial correction to fifth order) and chromatic aberrations corrected to the first order. Imaging data were collected at 24 °C with the Gatan K2 direct-detection camera operated in electron-counting mode. Images were recorded with total doses of 100 eÅ^{-2} to minimize sample damage. SEM and TEM samples were prepared via scooping films directly, or drop-casting film dispersions onto lacey carbon TEM grids purchased from Ted Pella. Infrared spectroscopy was conducted with a Bruker ALPHA ATR-FTIR. ATR-FTIR samples were prepared by scooping thick films directly onto aluminum foil. UV-Vis spectroscopic measurements were conducted on a Varian Cary 50 spectrophotometer. 2,5-bis(4-bromophenyl)-3-phenyl-4-(3-((triisopropylsilyl)ethynyl)phenyl)cyclopenta-2,4-dien-1-one [2], 2-(4-bromophenyl)-1,3-dioxolane [3] and unfunctionalized cGNRs[2] were synthesized following literature procedures.

3-phenyl-2,5-bis(4-(4,4,5,5-tetramethyl-1,3,2-dioxaborolan-2-yl)phenyl)-4-(3-((triisopropylsilyl) ethynyl)phenyl)cyclopenta-2,4-dien-1-one (**1**) An oven dried 200 mL Schlenk flask with reflux condenser was charged under N_2 with 2,5-bis(4-bromophenyl)-3-phenyl-4-(3-((triisopropylsilyl)ethynyl)phenyl)cyclopenta-2,4-dien-1-one (0.50 g, 0.69 mmol), $Pd(dppf)Cl_2$ (91 mg, 0.11 mmol), anhydrous KOAc (0.67 g, 6.80 mmol), and bis(pinacolato)diboron (0.68 g,

2.68 mmol) in anhydrous dioxane (80 mL). The reaction mixture was stirred for 5 h at 95 °C. The solvent was removed and the crude product was redissolved in CH_2Cl_2, washed with H_2O, saturated aqueous NaCl solution, dried over Na_2SO_4, and concentrated on a rotary evaporator. The crude product was passed through a plug of silica (EtOAc). The solvent was removed and the solid was sonicated in MeOH. This process was repeated until the MeOH filtrate was colorless, yielding **1** (0.47 g, 0.58 mmol, 84%) as a purple solid. ^{1}H NMR (400 MHz, $CDCl_3$, 22 °C) δ = 7.67–7.59 (m, 4H), 7.33 (dt, *J* = 7.7, 1.4, 1H), 7.29–7.18 (m, 7H), 7.13 (t, *J* = 7.7, 1H), 6.97–6.90 (m, 4H), 1.31 (m, 24H), 1.05 (m, 21H) ppm; ^{13}C {^{1}H} NMR (151 MHz, CD_2Cl_2, 22 °C) δ = 200.2, 155.8, 154.6, 134.8, 134.7, 134.2, 134.0, 133.7, 133.6, 133.5, 132.2, 129.9, 129.9, 129.8, 129.7, 129.3, 128.7, 128.6, 126.5, 126.1, 123.8, 106.9, 92.0, 84.4, 25.2, 19.0, 11.8 ppm; HRMS (ESI-TOF) m/z: $[C_{52}H_{62}B_2O_5Si]^+$ calcd. $[C_{52}H_{62}B_2O_5Si]$ 816.4547; found 816.4523.

2,5-bis(4'-(1,3-dioxolan-2-yl)-[1,1'-biphenyl]-4-yl)-3-phenyl-4-(3-((triisopropylsilyl)ethynyl) phenyl)cyclopenta-2,4-dien-1-one (**2**) A 25 mL Schlenk flask was charged with **1** (264 mg, 0.32 mmol), 2-(4-bromophenyl)-1,3-dioxolane[3] (224 mg, 0.98 mmol), and Aliquat 336 (6 drops) in 2M K_2CO_3 (3 mL) and dioxane (6 mL). The suspension was degassed via N_2 sparging for 30 min, after which $Pd(PPh_3)_4$ (60.4 mg, 0.053 mmol) was added under N_2. The reaction mixture was stirred at 100 °C for 20 h under N_2. The solution was cooled to 24 °C and diluted with CH_2Cl_2. The organic phase was washed with H_2O, saturated aqueous NaCl solution, dried over Na_2SO_4, and concentrated on a rotary evaporator. Column chromatography (SiO_2; 1–10% EtOAc/CH_2Cl_2) yielded **2** (189 mg, 0.22 mmol, 68%) as a purple solid. ^{1}H NMR (600 MHz, $CDCl_3$, 22 °C) δ = 7.64–7.60 (m, 4H), 7.56–7.50 (m, 8H), 7.37–7.33 (m, 5H), 7.31–7.28 (m, 1H), 7.27–7.23 (m, 2H), 7.17 (t, *J* = 7.7, 1H), 7.04–6.98 (m, 4H), 5.81–5.80 (m, 2H), 4.14–4.10 (m, 4H), 4.04–4.01 (m, 4H), 1.06–1.04 (m, 21H) ppm; ^{13}C {^{1}H} NMR (101 MHz, CD_2Cl_2, 22 °C) δ = 200.7, 155.4, 154.2, 141.8, 141.8, 140.3, 140.1, 138.0, 133.8, 133.6, 133.6, 132.2, 131.1, 130.6, 130.4, 129.9, 129.7, 129.3, 128.7, 128.7, 127.6, 127.5, 127.4, 127.3, 127.3, 127.2, 125.9, 125.5, 123.8, 106.8, 104.0, 92.0, 65.9, 18.9, 11.8 ppm; HRMS (ESI-TOF) m/z: $[C_{58}H_{56}O_5Si]^+$ calcd. $[C_{58}H_{56}O_5Si]$ 860.3892; found 860.3891.

2,5-bis(4'-(1,3-dioxolan-2-yl)-[1,1'-biphenyl]-4-yl)-3-(3-ethynylphenyl)-4-phenylcyclopenta-2,4-dien-1-one (**3**) An oven dried 25 mL Schlenk flask was charged under N_2 with **2** (61.3 mg, 0.07 mmol) in anhydrous THF (7 mL). A solution of TBAF (0.76 mL, 0.076 mmol, 0.1 M in THF) was added dropwise to the solution over a period of 5 min at 24 °C. The solution was stirred for an additional 10 min and the reaction was quenched with H_2O. The suspension was extracted with CH_2Cl_2 and the organic phase was washed with H_2O, dried over Na_2SO_4 and concentrated on a rotary evaporator. Column chromatography (SiO_2; 3:2 hexanes/EtOAc) yielded **3** (23.9 mg, 0.034 mmol, 48%) as a purple solid. ^{1}H NMR (500 MHz, CD_2Cl_2, 22 °C) δ = 7.64–7.60 (m, 4H), 7.56–7.50 (m, 8H), 7.41 (dt, *J* = 7.7, 1.2, 1H), 7.35–7.32 (m, 4H), 7.31–7.29 (m, 1H), 7.26–7.18 (m, 3H), 7.14–7.12 (m, 1H), 7.03–6.99 (m, 3H), 5.81–5.80 (m, 2H), 4.14–4.11 (m, 4H), 4.04–4.00 (m, 4H), 3.06 (s, 1H) ppm; ^{13}C {^{1}H} NMR (101 MHz, CD_2Cl_2, 22 °C) δ = 200.7, 155.3, 154.2, 141.8,

141.8, 140.3, 140.1, 138.0, 138.0, 134.3, 133.5, 133.1, 132.7, 131.1, 130.6, 130.3, 130.3, 129.8, 129.3, 128.9, 128.7, 127.6, 127.4, 127.3, 127.3, 127.2, 126.0, 125.4, 122.6, 104.0, 83.3, 78.3, 65.9 ppm; HRMS (ESI-TOF) m/z: $[C_{49}H_{36}O_5]^+$ calcd. $[C_{49}H_{36}O_5]$ 704.2557; found 704.2558

poly-**4** An oven dried 5 mL sealable tube was charged under N_2 with **3** (55.9 mg, 0.079 mmol) in Ph_2O (279.5 mg, 0.25 mL). The solution was degassed. The tube was sealed under N_2 and heated to 230 °C for 18 h. The solution was cooled to 24 °C, MeOH was added, and the precipitate was collected via centrifuge. The precipitate was dissolved in THF and reprecipitated with MeOH (1:2 THF/MeOH) and the resulting precipitate was collected via centrifuge. This process was repeated three times yielding **4** (46.8 mg, 87%) as a colorless solid. ^{1}H NMR (400 MHz, CD_2Cl_2, 22 °C) δ = 7.61–7.34 (m, 8H), 7.31–6.50 (m, 18H), 5.83–5.71 (br s, 2H), 4.16–3.89 (m, 8H)

poly-**5** A 20 mL vial was charged with **4** (83.1 mg, 0.12 mmol) in $CHCl_3$ (9 mL) under N_2. At 24 °C a solution of p-TsOH*H_2O (17.1 mg, 0.09 mmol) in acetone (2 mL) was added dropwise. The solution was stirred at 24 °C for 24 h. The reaction was quenched with saturated $NaHCO_3$ and the organic phase was collected, washed with H_2O, saturated aqueous NaCl solution, and dried over $MgSO_4$. The combined organic phases were concentrated and the polymer was precipitated via addition of MeOH. The solid was collected via centrifuge and reprecipitated from THF:MeOH (1:2). The crude polymer (66 mg, 0.10 mmol, 93%) was further purified via preparative GPC ($CHCl_3$), yielding a colorless solid (25.5 mg, 0.04 mmol, 36%) ^{1}H NMR (400 MHz, $CDCl_3$, 22 °C) δ = 10.06–9.85 (m, 2H), 7.94–7.29 (m, 10H), 7.21–6.45 (m, 16H) ppm

CHO-cGNR An oven dried 250 mL Schlenk flask was charged under N_2 with **5** (21.6 mg, 0.037 mmol) in anhydrous CH_2Cl_2 (120 mL). While sparging with N_2, a solution of $FeCl_3$ (352.2 mg, 2.17 mmol, 7 eq. per H) in anhydrous $MeNO_2$ (3.5 mL) was added at 0 °C. The reaction mixture was warmed to 24 °C and stirred for 72 h under a continuous stream of N_2. The black reaction mixture was quenched with MeOH and filtered over a membrane filter. The precipitate was washed with MeOH and THF. The solid was sonicated in (1:1) toluene/THF, filtered, then washed with THF, acetone, hexanes, ethyl acetate, and acetone yielding a dark purple precipitate CHO-cGNR (21.5 mg, 99%). Raman (powder) λ^{-1} = 253, 1277, 1332, 1603, 2688, 2892, 2942, 3216 cm^{-1}

cGNR-COF thin films A dispersion of CHO-cGNR (1.349 mg) in (1:1) *o*-DCB/$CHCl_3$ (4 mL), was added to a solution of benzidine (0.431 mg, 0.002 mmol) in (1:1) *o*-DCB/$CHCl_3$ (1 mL) and filtered through a pad of glass wool. A silanized vial was charged with the reaction mixture and carefully layered with a 5 mM $Sc(OTf)_3$ (aq.) solution. The vial was left undisturbed for 7 days, during which a gray film began to appear at the interface of the two liquids. The aqueous phase was gently removed by syringe and replaced with H_2O. The organic phase was gently removed and replaced with (1:1) *o*-DCB/$CHCl_3$. The film formed at the interface was scooped onto a substrate. The film was washed by dipping the substrate into water, acetone then isopropyl alcohol.

cGNR-COF film powder A dispersion of CHO-cGNR (1.349 mg) in (1:1) *o*-DCB/$CHCl_3$ (4 mL), was added to a solution of benzidine (0.431 mg, 0.002 mmol) in (1:1) *o*-DCB/$CHCl_3$ (1 mL) and filtered through a pad of glass wool. A silanized vial was charged with the reaction mixture and carefully layered with a 5 mM $Sc(OTf)_3$ (aq.) solution. The vial was left undisturbed for 7 days, during which a gray film began to appear at the interface of the two liquids. The aqueous phase was gently removed by syringe and replaced with H_2O. The organic phase was gently removed and replaced with (1:1) *o*-DCB/$CHCl_3$. A maximum amount of aqueous and organic phase was removed without disturbing the film. The interface suspended film was quickly poured into an excess of acetone. The film suspension was allowed to settle and the majority of the acetone was removed and replaced with fresh acetone. This process was repeated four times and the film dispersion were stored in acetone.

Liquid-phase exfoliation of cGNR-COF films A dispersion of cGNR-COF films in acetone (2–3 drops) was added to *o*-DCB (1 mL) and the suspension was sonicated for 15 min. The resulting dispersion was drop-cast onto the desired substrate at 24 °C and the solvent was removed under a stream of N_2. The substrate was gently rinsed with water, acetone, isopropyl alcohol, and dried under a stream of N_2.

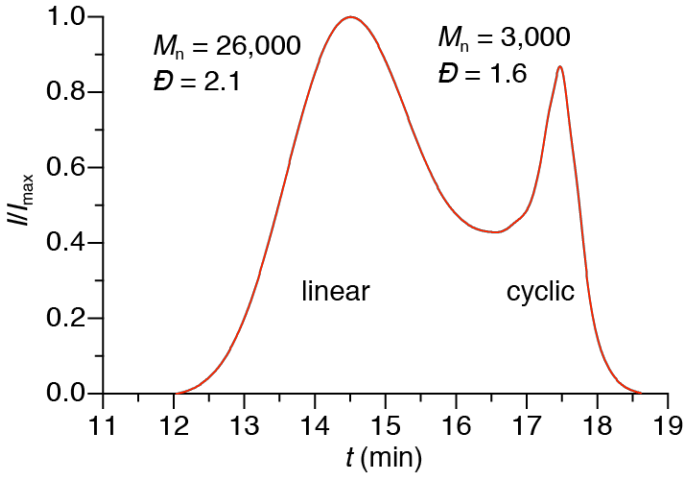

Figure S1. SEC trace ($CHCl_3$) of crude polyphenylene **4** containing linear polymers and cyclic oligomers.

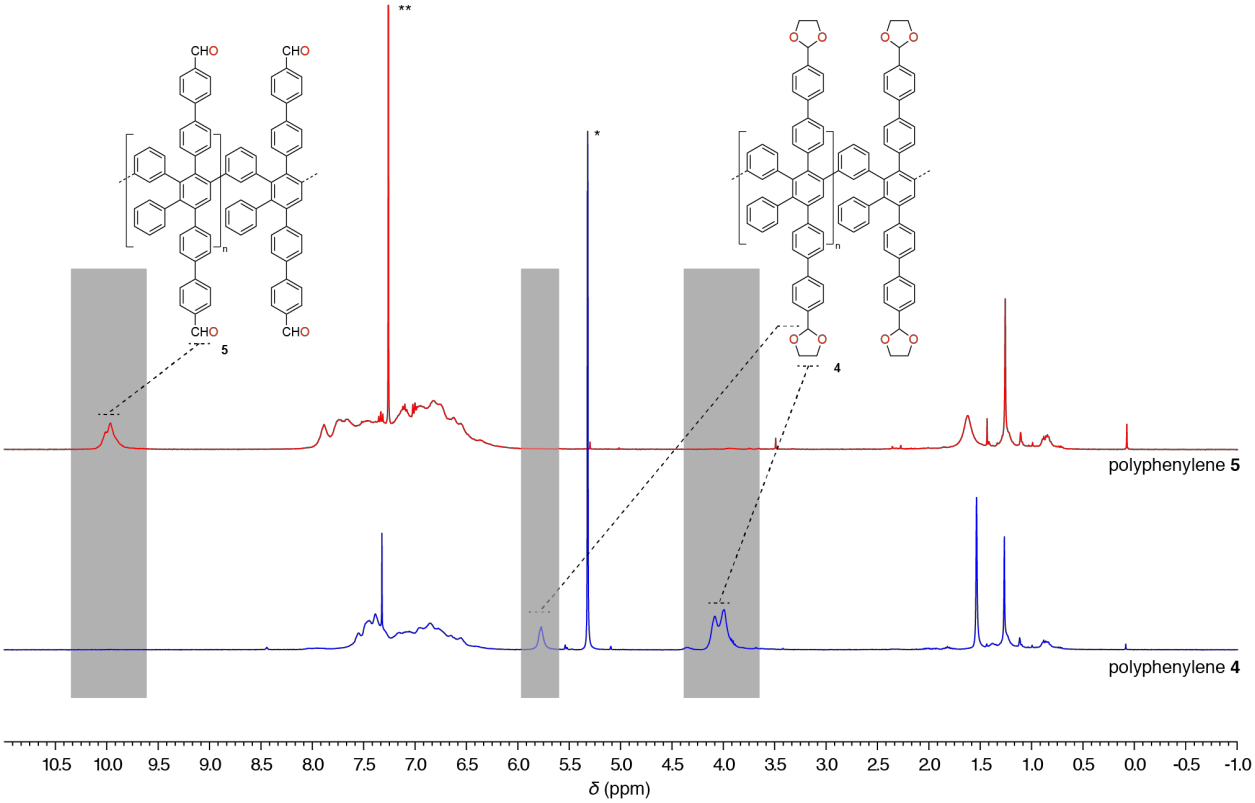

Figure S2. ^{1}H-NMR (400 MHz, CD_2Cl_2) of polyphenylene **4** (blue), and ^{1}H-NMR (400 MHz, $CDCl_3$) of polyphenylene **5** (red) following deprotection of the acetal groups. (* residual CH_2Cl_2, ** residual $CHCl_3$)

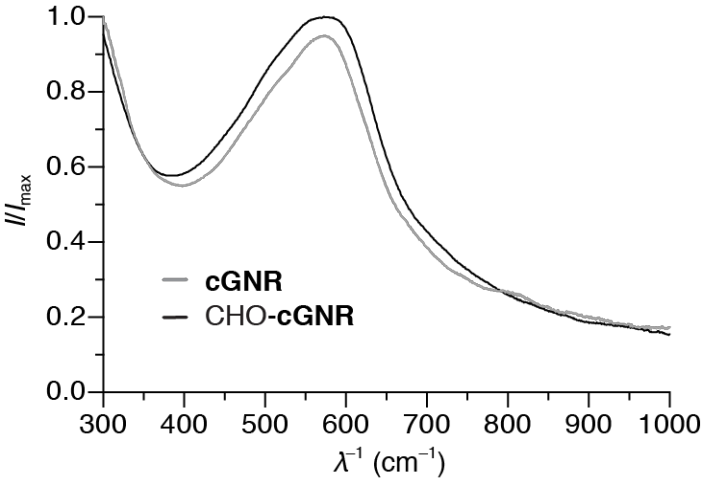

Figure S3. UV/vis absorption spectrum of unfunctionalized cGNR and CHO-cGNR dispersions in N-methylpyrrolidone (NMP).

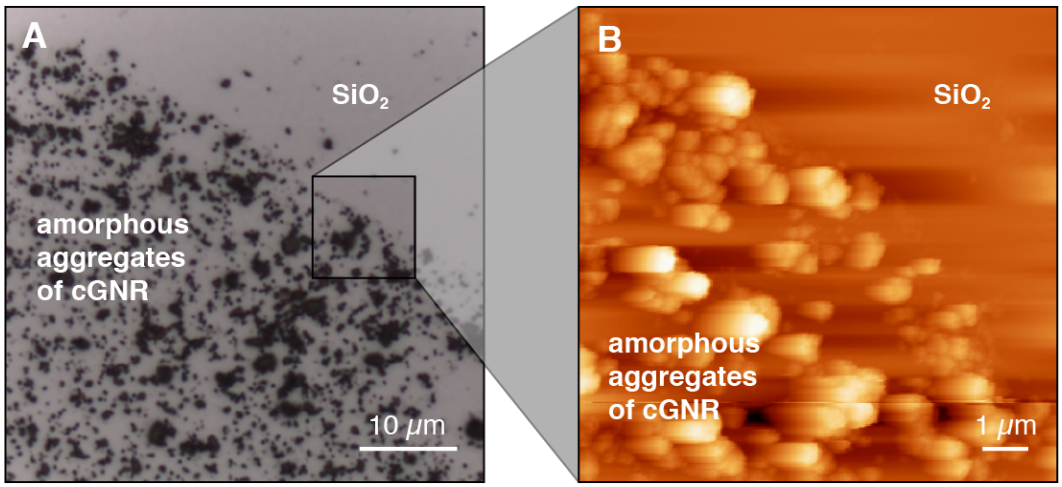

Figure S4. (A) Optical microscope image of a SiO_2 substrate after scooping the liquid-liquid interface of a negative control experiment with unfunctionalized cGNRs (cGNRs without aldehyde functional groups lining the edges). (B) Ambient AFM image of the same region of the substrate. While the surface is covered with large amorphous cGNR aggregates collecting at the liquid-liquid interface no crystalline film boundary can be observed in the sample.

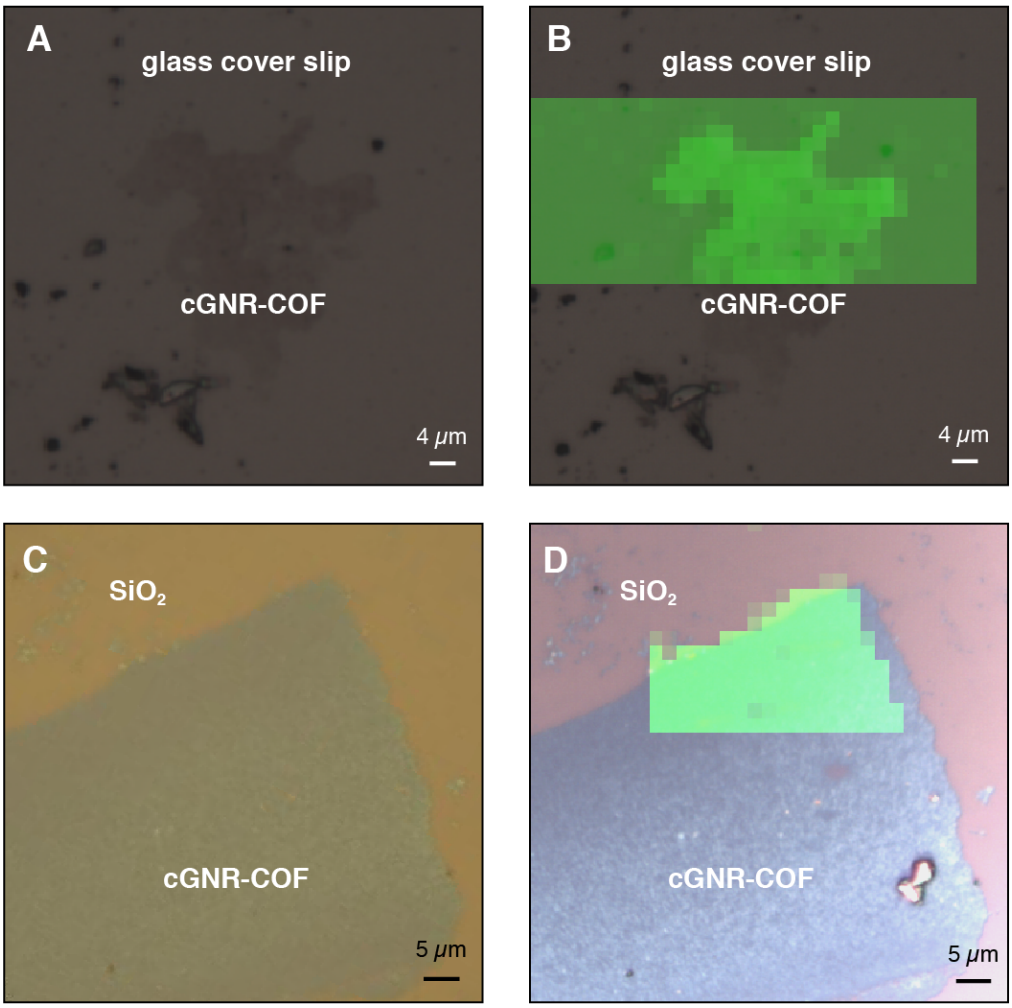

Figure S5. (A) Optical microscope images of a cGNR-COF thin films on a glass slide. (B) Raman map of G-peak intensity overlaid on the microscope image in A. (C) Optical microscope images of a cGNR-COF thin films on SiO_2. (B) Raman map of G-peak intensity overlaid on the microscope image in C.

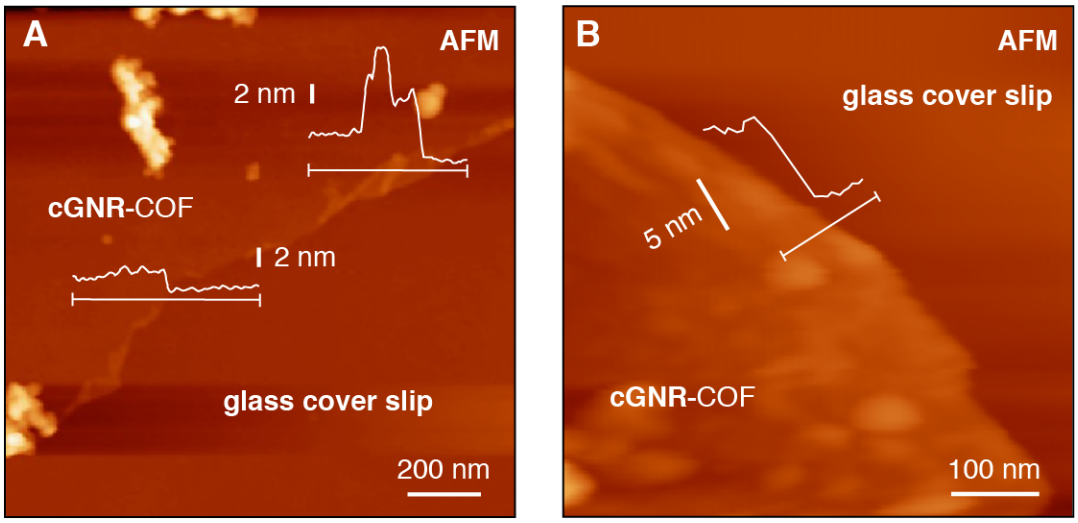

Figure S6. (A) Ambient AFM of cGNR-COF film on a glass cover slip showing homogenous film thickness of ~2 nm. (B) Ambient AFM of cGNR-COF film on a glass cover slip showing homogenous film thickness of ~8 nm.

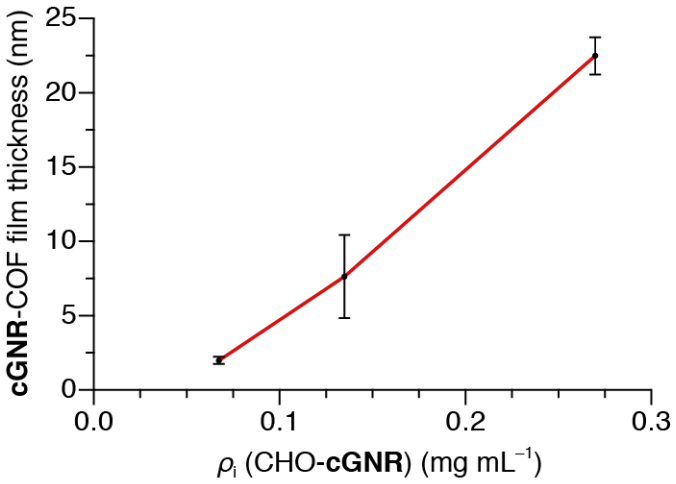

Figure S7. cGNR-COF film thickness as a function of CHO-cGNR mass concentration (ρ_i); film thicknesses were determined after transfer using ambient AFM.

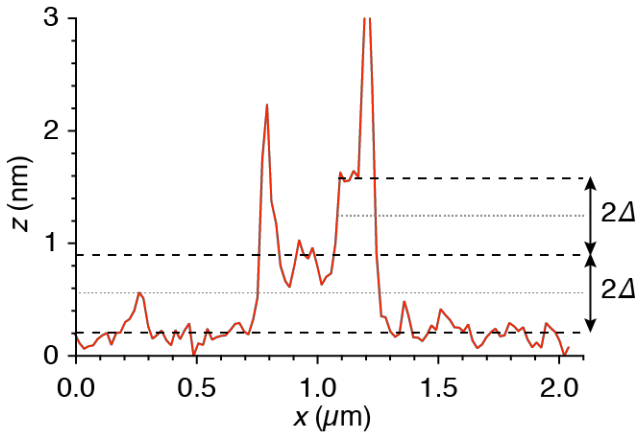

Figure S8. AFM topographic trace of liquid-phase exfoliated cGNR-COF on SiO_2. *z*-height profile shows a step-edge transition from a bilayer to a tetralayer flake.

Table S1. Structural Model for cGNR-COF

cGNR-COF			
Triclinic, $P\bar{1}$ a = 5.0000 Å, b = 7.4000 Å, c = 25.5000 Å α = 100°, β = 90°, γ = 90°			
Atom	***x***	***y***	***z***
C1	0.29413	0.20248	0.04067
C2	0.09533	0.24133	0.08105
C3	0.27601	–0.11706	0.04717
C4	0.07798	–0.07794	0.08740
C5	0.98279	0.10117	0.10535
C6	0.39157	0.02162	0.02217
C7	0.66520	0.28812	0.16958
N8	0.77595	0.13195	0.14724
C9	0.41257	–0.21965	0.41913
C10	0.20870	–0.19678	0.45897
C11	0.51459	0.26045	0.39936
C12	0.10312	0.31701	0.47982
C13	0.71691	0.24226	0.35975
C14	0.14755	–0.49083	0.27373
C15	0.34666	–0.51776	0.23359
C16	0.40930	0.10956	0.41977
C17	0.20532	0.13903	0.45962
C18	0.51633	–0.39740	0.39895
C19	0.10143	–0.34471	0.48017
C20	0.71948	–0.43134	0.35908
C21	0.14582	0.18477	0.27476
C22	0.34612	0.15797	0.23440
C23	0.45061	0.30667	0.21290
C24	0.82310	0.39154	0.33881
C25	1.04090	0.36140	0.29548
C26	0.59240	–0.44461	0.57963
C27	0.79415	–0.46851	0.54017
C28	0.49465	0.07002	0.59898
C29	0.89539	0.01188	0.52069
H30	0.38160	0.31833	1.02185
H31	1.02333	0.38825	0.09448
H32	0.34191	–0.26594	0.03505
H33	–0.00948	–0.19354	0.10634
H34	0.72846	0.42199	0.15681
H35	1.06905	–0.34692	0.28936
H36	0.42831	–0.39551	0.21691

H37	0.06465	0.06242	0.29146
H38	0.42528	0.01419	0.21883
H39	0.80250	0.10116	0.34310
H40	0.80779	–0.31253	0.34171

References

(1) Ilavsky, J. Nika: Software for Two-Dimensional Data Reduction. *J. Appl. Crystallogr.* **2012**, *45*, 324–328.

(2) Rogers, C.; Perkins, W. S.; Veber, G.; Williams, T. E.; Cloke, R. R.; Fischer, F. R. Synergistic Enhancement of Electrocatalytic CO2 Reduction with Gold Nanoparticles Embedded in Functional Graphene Nanoribbon Composite Electrodes. *J. Am. Chem. Soc.* **2017**, *139*, 4052–4061.

(3) Wang, B.; Li, P.; Yu, F.; Chen, J.; Qu, Z.; Han, K. A Near-Infrared Reversible and Ratiometric Fluorescent Probe Based on Se-BODIPY for the Redox Cycle Mediated by Hypobromous Acid and Hydrogen Sulfide in Living Cells. *Chem. Commun.* **2013**, *49*, 5790.